

# Anatase TiO<sub>2</sub> nanocrystals enclosed by well-defined crystal facets and their application in dye-sensitized solar cell

Cite this: *CrystEngComm*, 2013, 15, 516

Dapeng Wu,<sup>ab</sup> Zhiyong Gao,<sup>ab</sup> Fang Xu,<sup>a</sup> Jiuli Chang,<sup>a</sup> Shuyan Gao<sup>a</sup> and Kai Jiang<sup>\*ab</sup>

Anatase TiO<sub>2</sub> nanocrystals enclosed by well-defined {101} and {001} crystal facets were prepared *via* a facile hydrothermal method using H<sup>+</sup> exchanged potassium titanate nanowires (H-KTNWs) as precursors. The size and shape of the nanocrystals could be tuned by simply altering the precursor dosage and the NH<sub>4</sub>F concentration. The photovoltaic tests show that with decreasing of particles size, the dye-sensitized solar cell (DSSC) exhibits lower open circuit voltage ( $V_{oc}$ ) and fill factor (FF) due to the increased grain boundaries. However, because of the high short circuit current density ( $J_{sc}$ ) stemming from the enhanced dye loading capacity, the power conversion efficiency (PCE) was promoted. Moreover, the shape effect on the DSSC performance was evaluated by comparing the nanocrystals with similar surface area but different shapes. The cell derived from truncated octahedrons exposing ~25% {001} facets shows a ~10% PCE improvement compared with the cell derived from octahedrons exposing ~94% {101} facets. Based on the optical and recombination dynamic tests, the enhanced  $J_{sc}$ ,  $V_{oc}$  and FF could be ascribed to the enhancement in light scattering effect and suppressed electron recombination, which may result from the improved connectivity of the adjacent nanoparticles because it is energetically favourable for the truncated octahedrons to be linked together by the high energy {001} facets.

Received 7th September 2012,  
Accepted 27th October 2012

DOI: 10.1039/c2ce26454d

[www.rsc.org/crystengcomm](http://www.rsc.org/crystengcomm)

## 1 Introduction

Inorganic single crystals with elaborately engineered size and shape have attracted tremendous research interest because the surface conditions including the bond structure, surface tension and atom arrangement determine the physical and chemical performances of the material.<sup>1–5</sup> TiO<sub>2</sub> represents a versatile wide band gap semiconductor and received intensive research focus in the territories of water splitting, photocatalysis, gas-sensing and energy conversion/storage.<sup>6–10</sup> Recently, anatase TiO<sub>2</sub> nanocrystals exposing particular crystal facets were designed and prepared with different strategies. It was found that the anatase nanocrystals exposing high energy {001} or {100} facets possess improved catalytic, water splitting, lithium storage and solar energy conversion performances compared with the regular octahedrons enclosed by the inert {101} facets.<sup>11–24</sup>

Dye-sensitized solar cells (DSSCs) have been intensively studied for the past two decades as a low-cost and high efficient device to harness the green, abundant and renewable solar energy.<sup>25,26</sup> Anatase TiO<sub>2</sub> nanocrystals were considered

the best photoanode material for DSSCs because of its suitable energy band structure, pleasant long term stability against photo/chemical corrosion and sophisticated size/shape engineering strategies.<sup>27–34</sup> As for the nanoporous photoanode film of DSSCs, the particle size of the photoanode materials is of the foremost importance because it determines the dye loading capacity of the film at a given thickness. Although the particles with smaller size could substantially increase the accessible surface area and thus enhance the dye loading capacity, the decreased size would bring forth more undesired grain boundaries. Therefore, the increased trap states at the particle interfaces and the reduced connectivity of the film would prolong the electron residence time in traps and increase the length of electron diffusion, which boosts the recombination opportunities between the injected photoelectrons and the oxidized dye molecules or the electron acceptors in electrolyte.<sup>35–38</sup> On the other hand, TiO<sub>2</sub> nanocrystals with different shapes might also induce variation in the DSSC performances. Yu *et al.* firstly evaluated the shape effect *via* comparing the DSSCs derived from nanosheets exposing a high percentage of {001} facets and the regular octahedrons enclosed with {101} facets.<sup>22</sup> They found that the cell derived from highly crystallized anatase nanosheets exhibits much higher  $J_{sc}$  and PCE compared with the cell based on the regular octahedrons. The enhancement is mainly attributed to the promoted electrolyte diffusion rate and the improved crystal-

<sup>a</sup>School of Chemistry and Chemical Engineering, Henan Normal University, Xinxiang, P. R. China

<sup>b</sup>Engineering Technology Research Center of Motive Power and Key Materials of Henan Province, Henan Key Laboratory of Photovoltaic Materials, Xinxiang, Henan 453007, P. R. China. E-mail: [jiangkai6898@126.com](mailto:jiangkai6898@126.com); Fax: +86 3733326209

linity of the nanosheets. Lu *et al.* investigated the performance of the cells derived from the anatase nanocrystals exposing different percentages of {001} facets.<sup>23</sup> They found the sample exposing ~80% of {001} facets possesses the best photo-voltage performances, and the improvement was believed to result from the suppressed recombination rate. These works all aimed to evaluate the shape effects of the anatase TiO<sub>2</sub> nanocrystals on the PCE of DSSCs. However, the size of the products in these comparisons is not considered and controlled.<sup>24</sup> Therefore, the PCE differences may simply result from the variations of the particle size (specific surface area) and the crystallinity.

Herein, we employed a simple hydrothermal method to prepare anatase TiO<sub>2</sub> nanocrystals with different sizes and shapes (octahedrons exposing {101} facets and the truncated octahedrons exposing the {001} facets). Moreover, the nanocrystals were deposited as photoanode films to study their DSSC performances. Particularly, a set of octahedrons and truncated octahedrons with similar size and surface area was deliberately selected for comparison. It was shown that the cell based on truncated octahedrons (with surface area of 43.1 m<sup>2</sup> g<sup>-1</sup>) exposing ~25% {001} facets demonstrates a PEC of 7.4% which experiences a ~10% enhancement compared with 6.7% of the cell derived from the octahedrons dominated by the inert {101} facets and with surface area of 43.7 m<sup>2</sup> g<sup>-1</sup>. Based on the optical and electron recombination dynamic investigations, the film composed of truncated octahedrons possesses a better scattering effect in the visible range. Moreover, due to the high surface free energy, the adjacent truncated octahedron are more inclined to fuse together by coupling the high energy {001} facets, which may result in fewer grain boundaries and improved connectivity of the nanoporous film. Therefore, higher  $J_{sc}$ ,  $V_{oc}$  and FF were demonstrated, which finally leads to the PCE enhancement.

## 2 Experimental section

### 2.1 Preparation of the H-KTNWs

The potassium titanate nanowires (KTNWs) were firstly prepared by hydrothermal reaction of P25 powder (Degussa) in KOH solution.<sup>39</sup> Briefly, 2 g P25 was dispersed in 80 mL of 10 M KOH solution and sealed tightly in a Teflon-lined autoclave. After reacting at 200 °C for 24 h and cooling to room temperature, the white precipitate was separated by centrifugation and subsequently washed with deionized water several times until the pH value of the supernatant was reduced to less than 10. The as-prepared H-KTNWs were ion-exchanged in 0.1 M HNO<sub>3</sub> with agitating for several hours and then isolated by centrifugation. This exchange step was repeated several times until the pH value of the supernatant equalled about 7. The obtained H-KTNW were washed with deionized water and absolute ethanol, dried at 60 °C in vacuum and stored for later use.

### 2.2 Preparation of the anatase TiO<sub>2</sub> nanocrystals

**PREPARATION OF THE OCTAHEDRONS.** A certain amount of the H-KTNWs was dispersed in 40 mL deionized water and sealed

in a Teflon-lined autoclave. After reacting at 200 °C for 24 h, the white precipitate was separated by centrifugation and subsequently washed with deionized water and ethanol. In order to obtain octahedrons with different size, the H-KTNW dosage was changed to 0.05 g, 0.1 g and 0.2 g. The samples are accordingly denoted as 0.05O, 0.1O and 0.2O, respectively.

**PREPARATION OF THE TRUNCATED OCTAHEDRONS.** 0.1 g H-KTNWs was dispersed in 40 mL NH<sub>4</sub>F aqueous solution and sealed in a Teflon-lined autoclave. After reacting at 200 °C for 24 h, the white precipitate was separated by centrifugation and subsequently washed with deionized water and ethanol. In order to control the size of the truncated octahedrons, the NH<sub>4</sub>F concentration was altered to 0.05, 0.1 and 0.15 M. The samples are accordingly denoted as 0.05TO, 0.1TO and 0.2TO, respectively.

### 2.3 Material characterization

The products were characterized by field-emission scanning electron microscopy (FESEM, HITACHI, S4800), transmission electron microscopy (TEM, FEI Tecnai F30), X-ray powder diffraction (XRD, Rigaku D/max-2500 diffractometer with Cu K $\alpha$  radiation,  $\lambda$  = 0.1542, 40 kV, 100 mA) and Brunauer–Emmett–Teller (BET, Micrometrics ASAP 2010).

### 2.4 Fabrication of the DSSCs

**PREPARATION OF THE PHOTOANODE.** Hydroxypropyl cellulose (Aldrich) was added to diethylene glycol with a concentration of ~10 wt% to prepare the paste which was added in the stock wet TiO<sub>2</sub> nanocrystalline product (containing ~15% net TiO<sub>2</sub>) in a proportion of ~40% of TiO<sub>2</sub> weight. The mixture was vigorously stirred to obtain the slurry. The nanocrystal slurries were spread onto fluorine-doped tin oxide (FTO) glass substrate (TEC-8, LOF) with adhesive tape to control the film thickness. After drying in air, the film was heated up to 500 °C at a ramping rate of 5 °C min<sup>-1</sup> and maintained for 30 min.

**PREPARATION OF THE DSSCs.** After cooling to 80 °C, the films were sensitized in *cis*-bis(isothiocyanato)bis(2,2'-bipyridyl-4,4'-dicarboxylate) ruthenium(II)bis-tetrabutylammonium (N719, Solaronix SA, Switzerland) ethanol solution ( $3 \times 10^{-4}$  M) for 24 h.

The photoanodes were then sandwiched together with platinized FTO counter electrodes and electrolyte was then injected into the cell from the edges by capillary. The content of the electrolyte is 0.05 M LiI, 0.03 M I<sub>2</sub>, 0.5 M *tert*-butylpyridine, 0.1 M GuNCS and 1 M BMII in a mixture solvent of 85% acetonitrile and 15% valeronitrile.

### 2.5 Photovoltage measurements

The photocurrent–voltage ( $I$ – $V$ ) measurements were performed on a Keithley 4200 semiconductor characterization system using simulated AM 1.5 sunlight with an output power of 100 mW cm<sup>-2</sup> produced by a solar simulator (Newport 69911). The open circuit voltage decay (OCVD) measurement was performed under the open circuit condition and the voltage decay was then measured in function of the time after the illumination was cut off. Incident monochromatic photo-to-electron conversion efficiency (IPCE) was measured on Keithley 2000 source meter under the irradiation of 150 W tungsten lamp with 1/4 m monochromator (Spectral Product

DK240). The optical diffuse reflection spectra were recorded by a spectrophotometer (HITACHI U-4100). Electrochemical impedance spectroscopy (EIS) was performed in the dark on a potentiostat (EG&G, M283) equipped with a frequency response detector (EG&G, FRD100). The spectra were scanned with a bias voltage of  $-800$  mV and in a frequency ranging from  $100$  kHz to  $100$  MHz. The alternating voltage amplitude was set at  $10$  mV and the impedance parameters were obtained by fitting the spectra in Zsimpwin software.

### 3 Results and discussion

#### 3.1 Shape and size control

One dimensional titanate nanofibers derived from the alkali treatment of  $\text{TiO}_2$  particles represent a group of promising precursors to prepare high quality  $\text{TiO}_2$  crystals. By exchanging the alkali ions with protons for H-titanate, followed by hydrothermal transformation, the fibers were destroyed by bond cleavage and  $\text{TiO}_2$  crystals with high thermal stability and various structures/morphologies were prepared.<sup>40–47</sup> Fig. 1a and b show that the H-KTNWs are prepared in high yield and possess a one dimensional structure. The wire-like product is several micrometers in length and tens of nanometers in diameter. Moreover, the XRD displayed in Fig. 1c indicates that the as-formed H-KTNWs have similar diffraction peaks to the  $\text{K}_2\text{Ti}_6\text{O}_{13}$  structure (monoclinic  $C2/m$  JCPDS 40-0403, shown as the standard value), suggesting the ion-exchange would not destroy the Ti–O–Ti framework.<sup>39,43</sup>

Figs. 2a–c show the SEM images of  $\text{TiO}_2$  nanocrystals prepared in aqueous solution with different precursor dosages. In the pure water system, only octahedrons enclosed by well-defined  $\{101\}$  facets are observed. It is obvious that with decreasing precursor dosage from  $0.2$  g,  $0.1$  g to  $0.05$  g, the average particle size of 0.2O, 0.1O and 0.05O is gradually decreased. In addition, based on the Brunauer–Emmett–Teller (BET) measurements, the surface area of the samples is

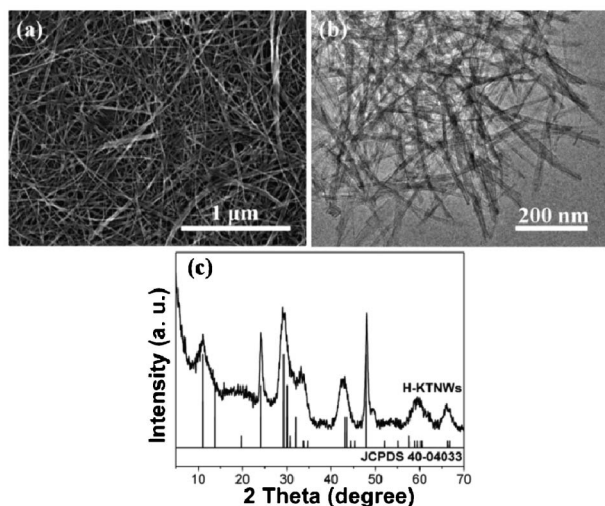


Fig. 1 SEM image (a), TEM image (b) and XRD pattern (c) of the as-prepared H-KTNWs.

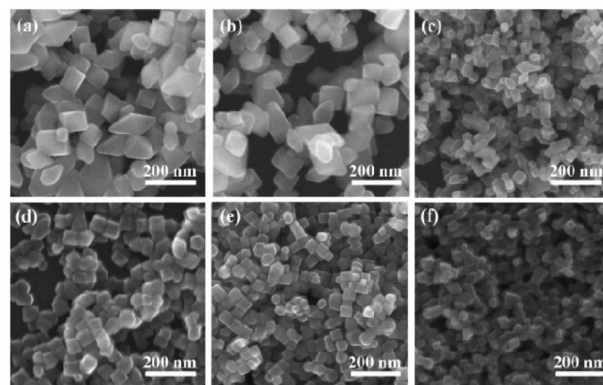


Fig. 2 SEM images of the as-prepared  $\text{TiO}_2$  nanocrystals: octahedrons prepared with H-KTNWs dosage of (a)  $0.2$  g, (b)  $0.1$  g and (c)  $0.05$  g; truncated octahedrons prepared with  $\text{NH}_4\text{F}$  concentration of (d)  $0.2$  M, (e)  $0.1$  M and (f)  $0.05$  M.

increased from  $38.6$ ,  $38.7$  to  $43.6$   $\text{m}^2 \text{g}^{-1}$ , respectively. Fig. 2d–f display the  $\text{TiO}_2$  truncated octahedrons prepared with  $0.1$  g precursor dosage and different  $\text{NH}_4\text{F}$  concentrations. In the  $\text{NH}_4\text{F}$  system, the as-prepared truncated octahedrons all have more uniform size distributions compared with octahedrons. In addition, decreasing the  $\text{NH}_4\text{F}$  concentrations from  $0.2$ ,  $0.1$  to  $0.05$  M, it is interesting to find that the particle size of 0.2TO, 0.1TO and 0.05TO is gradually reduced. The BET measurement indicates the surface areas of the samples increase accordingly from  $40.8$ ,  $43.1$  to  $47.9$   $\text{m}^2 \text{g}^{-1}$ .

The samples of 0.05O and 0.1TO with similar surface areas but different shapes were further characterized by the TEM and XRD investigations. Fig. 3 shows the TEM images of the samples. Fig. 3a shows an individual octahedron from 0.05O, the angle between the two crystal planes is  $\sim 43.4^\circ$  which is in accordance with the angle between the  $(101)$  and the  $(\bar{1}01)$

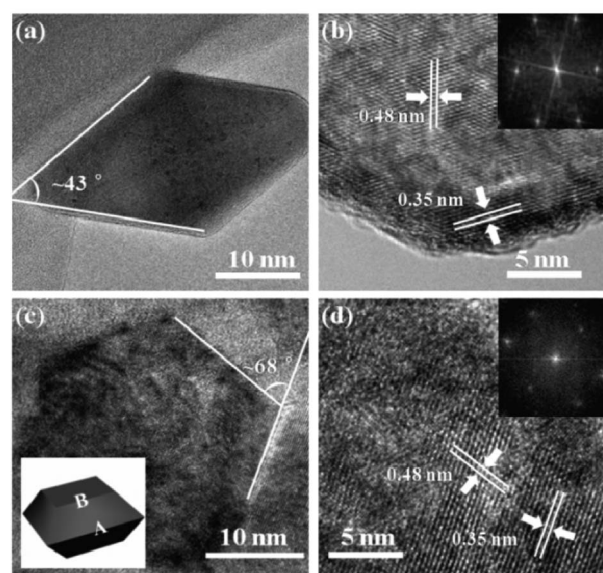
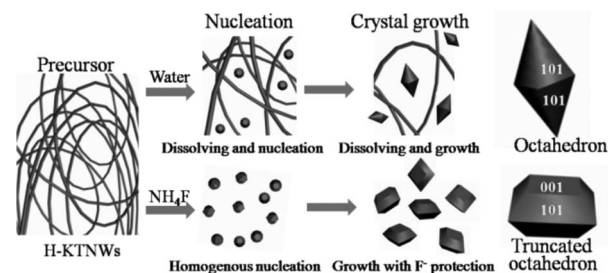


Fig. 3 TEM images of the samples (a, b) 0.05O and (c, d) 0.1TO. The insets are the corresponding FFT images.



facets.<sup>48</sup> Moreover, the HRTEM image shown in Fig. 3b displays two sets of lattice fringes and the interplanar spacing could be measured as 0.48 nm and 0.35 nm, which are in accordance with the (001) and (101) facets, respectively. The longitude (001) lattice fringes are evidence that the octahedron grows along the  $\langle 001 \rangle$  crystallographic orientation. Therefore, we can conclude that the octahedron is enclosed predominately by the thermodynamically stable {101} facets. Moreover, it should be noted that for the octahedrons, the {001} exposing percentage is generally less than 6%, according to the Wulff construction.<sup>49</sup> Fig. 3c depicts an individual truncated octahedron, the angle between the truncated plane and the lateral plane is  $\sim 68.3^\circ$  which matches well with the angle between the {001} and {101} facets.<sup>48</sup> As for 0.1TO, the HRTEM displayed in Fig. 3d shows the lattice fringe parallel with the truncated plane has an interplanar spacing of 0.48 nm, indicating the truncated planes are the (001) facets. Therefore, the as-prepared truncated octahedrons are enclosed by two {001} facets and eight {101} facets. The inset fast Fourier transfer (FFT) images further confirm the structure of the samples. In order to define the degree of truncation, the edges of the truncated octahedron are labeled as A and B as displayed in the inset of Fig. 3c. The B/A value could be measured as  $\sim 0.68$ , indicating the exposing percentage of the {001} facets is  $\sim 25\%$ .<sup>2,11,16</sup> As displayed in Fig. 4, the crystallinity and purity of the samples were investigated by XRD. All the diffraction peaks of the octahedrons and the truncated octahedrons could be indexed to anatase  $\text{TiO}_2$ , which matches well with the standard value (tetragonal,  $I4_1/amd$ , JCPDS 21-1272). Moreover, the peak intensities indicate that the as-prepared samples have a similar crystal quality. No diffraction peak belonging to impurities is detected, suggesting the high purity of the samples.

Scheme 1 depicts the possible growth process of the two types of nanocrystals. For the octahedrons prepared in pure water, the crystal growth experiences a dissolution and nucleation process, which has been described in detail in a previous report.<sup>39</sup> In this process, the H-KTNWs are gradually dissolved to release the  $\text{Ti}(\text{OH})_4$  units for the later nucleation



**Scheme 1** Illustration of the growth process for the  $\text{TiO}_2$  nanocrystals.

and growth of the nanocrystals. Moreover, the nucleation may occur at any time in the dissolving stage, which results in octahedrons with a broad size distribution. On the other hand, in the  $\text{NH}_4\text{F}$  system, because of the strong binding capacity of  $\text{F}^-$  ions towards the Ti atom, the  $\text{NH}_4\text{F}$  aqueous solution could completely dissolve the precursor in the initial stage by the cleavage of the Ti–O bonds of the precursor and the formation of Ti–F bonds in the solution.<sup>50</sup> When heated at high temperature, homogenous nucleation occurred in the solution, in which the nucleus would form in a short period of time. Therefore, the truncated octahedrons all have narrow size distributions. In addition, it is reasonable to anticipate that under higher  $\text{NH}_4\text{F}$  concentration, fewer nuclei could be formed in the initial stage because the Ti species could be sufficiently stabilized. Therefore, with lower nucleus numbers and the same Ti precursor, truncated octahedrons with greater particle size are formed in the reaction. Moreover, considering the Ti–F bonds can significantly reduce the surface free energy of the {001} facets to lower than that of the {101} facets,<sup>11</sup> the  $\text{F}^-$  ions could also function as the capping reagent to stabilize the high energy {001} facets and hinder the growth along the  $\langle 001 \rangle$  direction, which finally shapes the truncated octahedrons.

### 3.2 DSSCs performances

Considering samples 0.2O and 0.1O have the similar surface areas and morphologies, five samples were deposited as the photoanode films for the DSSCs test and the corresponding cells were labelled as Cell-0.1O, Cell-0.05O, Cell-0.2TO, Cell-0.1TO and Cell-0.05TO. The photoanode film thicknesses were all controlled at  $\sim 11 \mu\text{m}$  and the active film areas at  $\sim 0.16 \text{ cm}^2$ . The photocurrent–photovoltage ( $I$ – $V$ ) curves of the DSSCs are shown in Fig. 5 and the corresponding photovoltaic characteristics are summarized in Table 1. It is obvious that the smaller particle size would lead to higher surface area and thus higher dye loading capacity, which could directly contribute to the higher harvesting efficiency of the incident light and the higher  $J_{\text{sc}}$ . The enhanced  $J_{\text{sc}}$  is considered as the primary cause for the PCE improvement. However, the small particle size would also bring forth more grain boundaries in the nanoporous film, which results in more recombination opportunities and the increased inner series resistance of the cell.<sup>35,36</sup> Therefore, the  $V_{\text{oc}}$  and the FF of the cell are decreased with reducing the particle size.<sup>51</sup> In the comparison, the film thickness is relative thin ( $\sim 11 \mu\text{m}$ ). Thus, although the  $V_{\text{oc}}$  and FF are both slightly reduced, the substantially increased

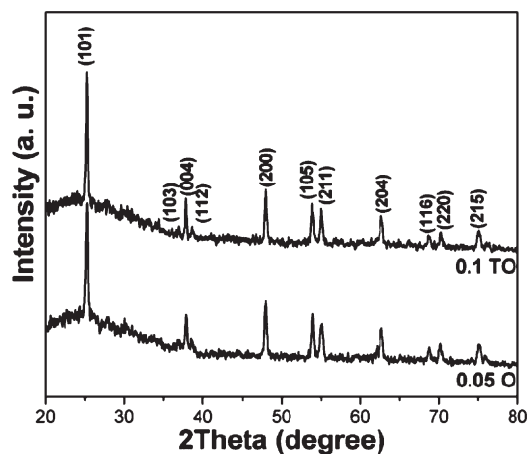


**Fig. 4** XRD patterns of the samples 0.05O and 0.1TO prepared in pure water and the  $\text{NH}_4\text{F}$  aqueous solution.

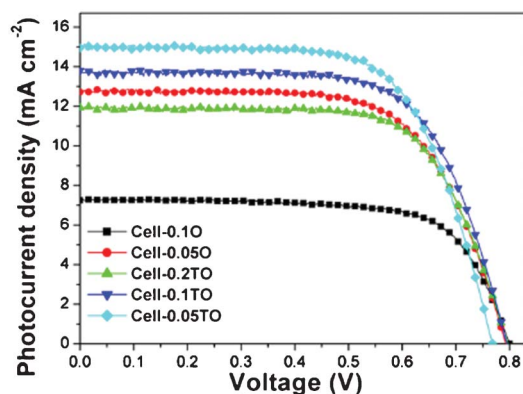


Fig. 5 *I*-*V* curves of the DSSCs based on the different photoanodes measured under one sun (AM 1.5 G, 100 mW cm<sup>-2</sup>).

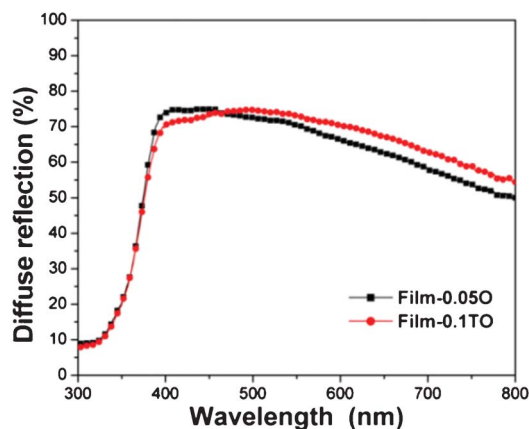


Fig. 6 The UV-vis diffuse reflection spectra of the as-prepared photoanode films.

$J_{sc}$  still leads to the improved overall PCE. Typically, when sample 0.05TO with the largest surface area was employed as the photoanode, Cell-0.05TO demonstrates the highest  $J_{sc}$  of 14.9 mA cm<sup>-2</sup> and PCE of 7.7%. On the contrary, Cell-0.1O with the lowest surface area finally evidences a low  $J_{sc}$  of 7.2 mA cm<sup>-2</sup> and PCE of 4.1%.

### 3.3 Shape effect on the photovoltaic performances

In order to gain insight into the shape effect between the octahedron and the truncated octahedron on the DSSCs performances, sample 0.05O and 0.1TO with similar surface areas but different shapes were selected for comparison. As displayed in Table 1, Cell-0.05O demonstrates a  $J_{sc}$  of 12.7 mA cm<sup>-2</sup>,  $V_{oc}$  of 792 mV and FF of 66.6%. As a result, the PCE reaches to 6.7%. In contrast, Cell-0.1TO shows a  $J_{sc}$  of 13.8 mA cm<sup>-2</sup>,  $V_{oc}$  of 794 mV and FF of 67.5%. Therefore, the PCE is enhanced to 7.4%, indicating a ~10% improvement over Cell-0.05O. As displayed in Fig. 6, the UV-vis diffuse reflection spectra were investigated to evaluate the scattering effects of the photoanode films. The reflectance of Film-0.05O derived from the octahedrons experiences a fast decrease in the visible region, which is a typical behavior of the nanocrystal based film.<sup>26,28,52</sup> However, the reflectance of Film-0.1TO is slightly improved to alleviate the downward trend, which may be ascribed to the unique structure of the truncated octahedrons. The improved scattering effect of the photoanode film helps to trap the incident light within the photoanode and finally contribute to the  $J_{sc}$  enhancement.<sup>53</sup> Moreover, the incident monochromatic photon-to-current conversion efficiency (IPCE) spectra provide straightforward evidence for the  $J_{sc}$  variations. Fig. 7 shows the IPCE spectra as a function of

wavelength for the two cells. Cell-0.1TO shows a higher IPCE value at the whole wavelength range compared with that of Cell-0.05O. Moreover, a clear IPCE peak is observed in Cell-0.1TO at the region of 600–700 nm, which is supposed to result from the enhanced scattering effect of the photoanode.

To further interpret the mechanism of shape effect on the PCE, the electron recombination dynamic was investigated. Fig. 8 shows the open circuit voltage decay (OCVD) tests.<sup>23</sup> The measurements were carried out under open circuit conditions. When the illumination was removed, considering no electron is transported through the external circuit, the photoinduced electrons are all recombine with the electron acceptors in the electrolyte. Therefore, the  $V_{oc}$  would follow an exponential decay during the recombination process. The dots shown in Fig. 8a represent the measured  $V_{oc}$  data points after the illumination was cut off. After fitting with exponential decay functions, the solid lines indicate that Cell-0.05O has an evidently faster  $V_{oc}$  decay, indicating a more rapid recombination compared with that of Cell-0.1TO. Based on previous work,<sup>54,55</sup> the electron recombination lifetime in function of  $V_{oc}$  could be obtained by differentiating the OCVD curves and then taking an inverse, which are displayed in Fig. 8b. Obviously, Cell-0.1TO exhibits higher electron lifetime in the whole voltage range than Cell-0.05O, indicating the nanoporous film composed of truncated octahedrons possess fewer grain boundaries and lower recombination rate.

Moreover, the cells were also characterized by electrochemical impedance spectra (EIS). Fig. 9a depicts the typical Nyquist plots of the EIS, and the inset is the equivalent circuit. Under the dark testing conditions, the electrons transport

Table 1 Photovoltaic performance of DSSCs (the active area for all the cells are ~0.16 cm<sup>2</sup>)

Cells	$J_{sc}$ , mA cm <sup>-2</sup>	$V_{oc}$ , mV	FF, %	PCE, %	Dye absorption, mol cm <sup>-2</sup>	Surface area, m <sup>2</sup> g <sup>-1</sup>
0.1O	7.2	800	71.1	4.1	$0.8 \times 10^{-7}$	38.6
0.05O	12.7	792	66.6	6.7	$1.48 \times 10^{-7}$	43.7
0.2TO	11.9	796	68.6	6.5	$1.20 \times 10^{-7}$	40.8
0.1TO	13.8	794	67.5	7.4	$1.41 \times 10^{-7}$	43.1
0.05TO	14.9	768	67.2	7.7	$1.60 \times 10^{-7}$	47.9

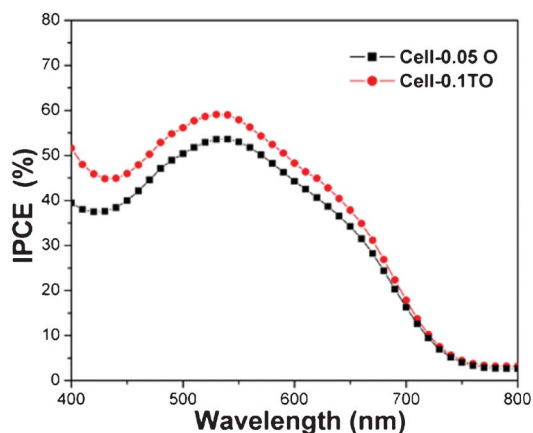


Fig. 7 The IPCE spectra of the as-prepared DSSCs.

through the film and react with the  $I_3^-$  in the electrolyte. Meanwhile,  $I^-$  is simultaneously oxidized to  $I_3^-$  at the counter electrode.<sup>56–58</sup> The major concern of the current research is the recombination resistance occurring at the  $TiO_2$ -dye-electrolyte interface, which could be fitted as  $R_{ct2}$ .<sup>59</sup> On the other hand, the  $R_{ct1}$  represents the charge transfer resistance ascribed to the process at the electrolyte-Pt counter electron interface.

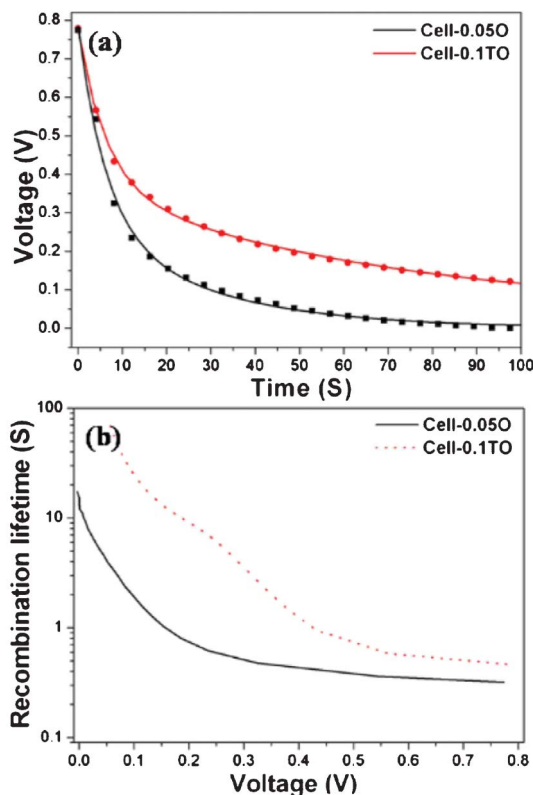


Fig. 8 The open circuit voltage decay (OCVD) tests of the two cells: (a) the  $V_{oc}$  decay curves after cut off the illumination, the dots are the experimental data points and the solid lines represent the fitted curves; (b) electron recombination lifetimes in function of the  $V_{oc}$ .

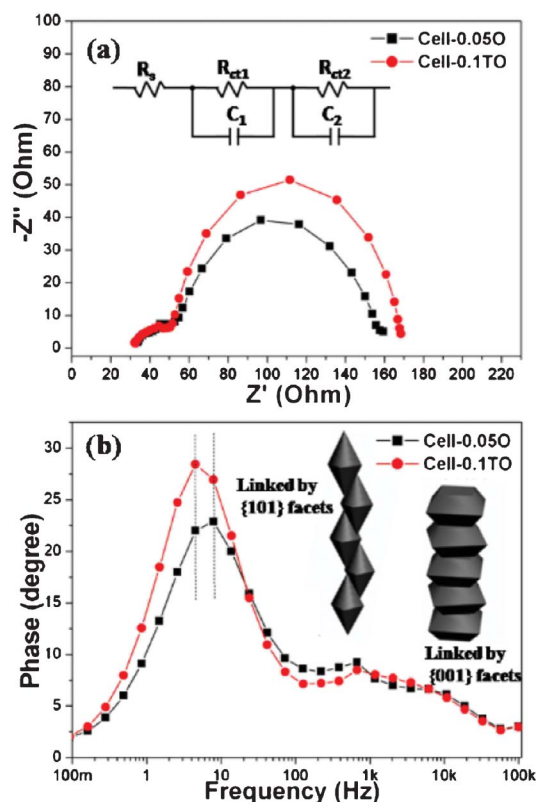


Fig. 9 The (a) Nyquist and (b) Bode phase plots of the EIS spectra for the cells. The inset in (a) is the equivalent circuit, while the inset in (b) is the illustration of the nanocrystals linked by different crystal facets.

Based on the inset equivalent circuit and the Zsimpwin software, Cell-0.1TO has a larger  $R_{ct2}$  (111.3  $\Omega$ ) compared with Cell-0.1TO (93.4  $\Omega$ ), indicating a slower electron recombination for the former cell. Fig. 9b shows the Bode phase plots of the EIS spectra. Moreover, the middle frequency peak of Cell-0.1TO is slightly shifted to the low frequency region, indicating a greater electron lifetime ( $\tau_{nEIS}$ ) compared with that of Cell-0.05 O. Based on the equation of  $\tau_{nEIS} = 1/\omega_{max} = 1/2\pi f_{max}$ ,<sup>60</sup> where  $f_{max}$  is the maximum frequency of the intermediate frequencies peak, Cell-0.1TO has a  $\tau_{nEIS}$  of  $\sim 35$  ms, indicating a 75% improvement than that of Cell-0.05 O ( $\sim 20$  ms). As we know, compared with free electrons in the conduction band, it is energetically favorable for the electrons confined in the trap states to recombine with the  $I_3^-$  in the electrolyte.<sup>55</sup> The longer electron lifetime in Cell-0.1TO reflects the lower trap state density in the cell system, indicating fewer grain boundaries and surface defects exist in the truncated octahedron based film framework.

The electron dynamic measurements of OCVD and EIS agree that Cell-0.1TO driving from  $TiO_2$  truncated octahedrons shows more effective suppression for the back reaction of the injected electron with the  $I_3^-$  in the electrolyte. As illustrated in the inset of Fig. 9b, considering the  $F^-$  ions adsorbed on the {001} facets could be removed by heat treatment,<sup>11</sup> it is reasonable to anticipate that adjacent truncated octahedrons are inclined to be linked together by

the exposed high energy {001} facets in the calcination process for photoanode fabrication. In contrast, the linkage of octahedrons can only be formed in a manner of eliminating the neighbouring low energy {101} facets, which is less thermodynamically feasible. As a result, compared with the octahedron nanoporous film, the film based on truncated octahedrons is expected to possess better interparticle connectivity and conductivity, which could possibly suppress the recombination and reduce the series resistance of the cell. Therefore, better  $J_{sc}$ ,  $V_{oc}$  and FF were achieved in Cell-0.1TO compared with Cell-0.05O.

## 4 Conclusions

In summary, well-defined anatase  $TiO_2$  octahedrons exposing ~94% {101} facets and the truncated octahedrons exposing ~25% {001} facets were prepared by hydrothermal treating of the H-KTNW precursor. The size and the overall surface area of the nanocrystals could be tuned by altering the precursor dosage or the  $NH_4F$  concentration. The DSSCs test shows the PCE is promoted steadily as decreasing of the particle size, which is ascribed to the high  $J_{sc}$  stemming from the enhanced dye loading capacity. Typically, the cell based on the truncated octahedron with the largest surface area demonstrates the highest PCE of 7.7%. Moreover, the shape effects on the DSSCs performance were intensively investigated by comparing two samples possessing similar surface area. Film-0.1TO comprised of truncated octahedrons shows enhanced scattering effect in the visible range compared with Film-0.05O derived from the octahedrons, which leads to a better harness of the incident light. Moreover, the OVCD test shows the Cell-0.1TO exhibits a longer  $\tau_n$  than that of Cell-0.05O, which may probably derive from the improve connectivity of the neighboring truncated octahedrons due to the exposed high energy {001} facets. Therefore, the suppressed recombination rate and the reduced series resistance of the cell result in an improved  $V_{oc}$  and FF. As a result, Cell-0.1TO demonstrates a PCE of 7.4%, indicating a ~10% enhancement compared with the octahedron cell (6.7%).

## Acknowledgements

This work is supported by National Natural Science Foundation of China (61204078 and 61176004), Basic and Frontier Research Programs of Henan Province (No. 092300410240 and No. 112300410094), Natural Science Foundation of Education Department of Henan Province (2010 B150012, 2011A150017).

## References

- 1 N. Tian, Z. Y. Zhou, S. G. Sun, Y. Ding and Z. L. Wang, *Science*, 2007, **316**, 732.
- 2 A. S. Barnard and L. A. Curtiss, *Nano Lett.*, 2005, **5**, 1261.

- 3 A. G. Thomas, *Phys. Rev. B: Condens. Matter*, 2003, **67**, 035110.
- 4 L. Kavan, M. Gratzel, S. E. Gilbert, C. Klemenz and H. J. Scheel, *J. Am. Chem. Soc.*, 1996, **118**, 6716.
- 5 A. Vittadini, A. Selloni, F. P. Rotzinger and M. Gratzel, *Phys. Rev. Lett.*, 1998, **81**, 2954.
- 6 A. Fujishima and K. Honda, *Nature*, 1972, **238**, 37.
- 7 C. J. Barbe, *J. Am. Ceram. Soc.*, 1997, **80**, 3157.
- 8 B. O'Regan and M. Gratzel, *Nature*, 1991, **353**, 737.
- 9 J. Chen, Y. Tan, C. Li, Y. L. Cheah, D. Luan, S. Madhavi, F. Boey, L. A. Archer and X. Lou, *J. Am. Chem. Soc.*, 2010, **132**, 6124.
- 10 X. Chen and S. S. Mao, *Chem. Rev.*, 2007, **107**, 2891.
- 11 H. G. Yang, C. H. Sun, S. Z. Qiao, J. Zou, G. Liu, S. C. Smith, H. M. Cheng and G. Q. Lu, *Nature*, 2008, **453**, 638.
- 12 H. G. Yang, G. Liu, S. Z. Qiao, C. H. Sun, Y. G. Jin, S. C. Smith, J. Zou, H. M. Cheng and G. Q. Lu, *J. Am. Chem. Soc.*, 2009, **131**, 4078.
- 13 X. Han, Q. Kuang, M. Jin, Z. Xie and L. Zheng, *J. Am. Chem. Soc.*, 2009, **131**, 3152.
- 14 F. Amano, O. O. Prieto-Mahaney, Y. Terada, T. Yasumoto, T. Shibayama and B. Ohtani, *Chem. Mater.*, 2009, **21**, 2601.
- 15 J. Pan, G. Liu, G. Lu and H. Cheng, *Angew. Chem., Int. Ed.*, 2011, **50**, 2133.
- 16 D. Zhang, G. Li, H. Wang, K. Chan and J. Yu, *Cryst. Growth Des.*, 2010, **10**, 1130.
- 17 J. Chen and X. Lou, *Electrochem. Commun.*, 2009, **11**, 2332.
- 18 J. Feng, M. Yin, Z. Wang, S. Yan, L. Wan, Z. Li and Z. Zou, *CrystEngComm*, 2010, **12**, 3425.
- 19 J. Zhu, S. Wang, Z. Bian, S. Xie, C. Cai, J. Wang, H. Yang and H. Li, *CrystEngComm*, 2010, **12**, 2219.
- 20 X. Yang, Z. Li, G. Liu, J. Xing, C. Sun, H. Yang and C. Li, *CrystEngComm*, 2011, **13**, 1378.
- 21 W. Yang, J. Li, Y. Wang, F. Zhu, W. Shi, F. Wan and D. Xu, *Chem. Commun.*, 2011, **47**, 1809.
- 22 J. Yu, J. Fan and K. L. Lv, *Nanoscale*, 2010, **2**, 2144.
- 23 X. Wu, Z. Chen, G. Lu and L. Wang, *Adv. Funct. Mater.*, 2011, **21**, 4167.
- 24 W. Yang, Y. Wang and W. Shi, *CrystEngComm*, 2012, **14**, 230.
- 25 M. Gratzel, *Nature*, 2001, **414**, 338.
- 26 M. Gratzel, *Inorg. Chem.*, 2005, **44**, 6841.
- 27 G. K. Mor, O. K. Varghese, M. Paulose, K. Shankar and C. A. Grimes, *Sol. Energy Mater. Sol. Cells*, 2006, **90**, 2011.
- 28 D. H. Chen, F. Z. Huang, Y. B. Cheng and R. A. Caruso, *Adv. Mater.*, 2009, **21**, 2206.
- 29 F. Sauvage, D. H. Chen, P. Comte, F. Z. Huang, Y. B. Cheng, R. A. Caruso and M. Gratzel, *ACS Nano*, 2010, **4**, 4420.
- 30 D. H. Chen, L. Cao, F. Z. Huang, P. Imperia, Y. B. Cheng and R. A. Caruso, *J. Am. Chem. Soc.*, 2010, **132**, 4438.
- 31 D. Kuang, J. Brillet, P. Chen, M. Takata, S. Uchida, H. Miura, K. Sumioka, S. M. Zakeeruddin and M. Gratzel, *ACS Nano*, 2008, **2**, 1113.
- 32 G. K. Mor, J. Basham, M. Paulose, S. Kim, O. K. Varghese, A. Vaish, S. Yoriya and C. A. Grimes, *Nano Lett.*, 2010, **10**, 2387.
- 33 Q. Chen and D. Xu, *J. Phys. Chem. C*, 2009, **113**, 6310.
- 34 D. Wu, F. Zhu, J. Li, H. Dong, Q. Li, K. Jiang and D. Xu, *J. Mater. Chem.*, 2012, **22**, 11665.
- 35 G. Schlichthorl, N. G. Park and A. J. Frank, *J. Phys. Chem. B*, 1999, **103**, 782.



- 36 L. Dloczik, O. Ileperuma, I. Lauermann, L. M. Peter, E. A. Ponomarev, G. Redmond, N. J. Shaw and I. Uhlendorf, *J. Phys. Chem. B*, 1997, **101**, 10281.
- 37 J. V. de Lagemaat and A. J. Frank, *J. Phys. Chem. B*, 2001, **105**, 11194.
- 38 K. D. Benkstein, N. Kopidakis, J. V. de Lagemaat and A. J. Frank, *J. Phys. Chem. B*, 2003, **107**, 7759.
- 39 J. Li, Y. Yu, Q. Chen, J. Li and D. Xu, *Cryst. Growth Des.*, 2010, **10**, 2111–2115.
- 40 Y. Yu and D. Xu, *Appl. Catal., B*, 2007, **73**, 166.
- 41 Y. Mao and S. S. Wong, *J. Am. Chem. Soc.*, 2006, **128**, 8217.
- 42 H. Zhu, Y. Lan, X. Gao, S. Ringer, Z. Zheng, D. Song and J. Zhao, *J. Am. Chem. Soc.*, 2005, **127**, 6730.
- 43 G. Du, Q. Chen, P. Han, Y. Yu and L. M. Peng, *Phys. Rev. B: Condens. Matter*, 2003, **67**, 035323.
- 44 F. Amano, T. Yasumoto, O. Prieto-Mahaney, S. Uchida, T. Shibayama and B. Ohtani, *Chem. Commun.*, 2009, 2311.
- 45 J. Li and D. Xu, *Chem. Commun.*, 2010, **46**, 2301.
- 46 J. Li, K. Cao, Q. Li and D. Xu, *CrystEngComm*, 2012, **14**, 83.
- 47 J. Li, H. Yang, Q. Li and D. Xu, *CrystEngComm*, 2012, **14**, 3019.
- 48 C. Howard, T. Sabine and F. Dickson, *Acta Crystallogr., Sect. B: Struct. Crystallogr. Cryst. Chem.*, 1991, **47**, 462.
- 49 M. Lazzeri, A. Vittadini and A. Selloni, *Phys. Rev. B: Condens. Matter*, 2001, **63**, 155409.
- 50 J. Yu, Q. Xiang, J. Ran and S. Mann, *CrystEngComm*, 2010, **12**, 872.
- 51 M. Kim, B. Kim and J. Kim, *ACS Appl. Mater. Interfaces*, 2009, **1**, 1264.
- 52 S. Ito, P. Chen, P. Comte, M. K. Nazeeruddin, P. Liska, P. Pechy and M. Gratzel, *Prog. Photovoltaics*, 2007, **15**, 603.
- 53 S. Hore, C. Vetter, R. Kern, H. Smit and A. Hinsch, *Sol. Energy Mater. Sol. Cells*, 2006, **90**, 1176.
- 54 A. Zaban, M. Greenshtein and J. Bisquert, *ChemPhysChem*, 2003, **4**, 859.
- 55 J. Bisquert, A. Zaban, M. Greenshtein and I. Mora-Sero, *J. Am. Chem. Soc.*, 2004, **126**, 13550.
- 56 Q. Wang, S. Ito, M. Gratzel, F. Fabregat-Santiago, I. Mora-Sero, J. Bisquert, T. Bessho and H. Imai, *J. Phys. Chem. B*, 2006, **110**, 25210.
- 57 D. Wu, Z. Gao, F. Xu, Z. Shi, W. Tao and K. Jiang, *CrystEngComm*, 2012, **14**, 7934.
- 58 J. Sheng, L. Hu, S. Xu, W. Liu, L. Mo, H. Tian and S. Dai, *J. Mater. Chem.*, 2011, **21**, 5457.
- 59 J. Liao, H. Lin, H. Chen, D. Kuang and C. Su, *J. Mater. Chem.*, 2012, **22**, 1627.
- 60 R. Kern, R. Sastrawan, J. Ferber, R. Stangl and J. Luther, *Electrochim. Acta*, 2002, **47**, 4213.